

Thermal Stresses in Multilayer Ceramic Capacitors: Numerical Simulations

GEOFFREY C. SCOTT, MEMBER, IEEE, AND GREG ASTFALK

Abstract—A model to characterize the development of thermal stresses in surface mounted multilayer ceramic capacitors (MLCC's) was presented previously. The work reported here concerns numerical simulations using the model. In particular, the model was used to investigate the effect of several important factors on the development of thermal stresses in MLCC's. These factors relate to the solder process temperature profile and MLCC printed wiring board (PWB) geometry and material properties. The results indicate that the peak temperature during wave solder and that the geometry and material properties of the MLCC termination have a major influence on the development of thermal stresses in MLCC's. These factors are actually a small portion of all of the factors commonly thought to have a significant influence on thermal stress development.

NOMENCLATURE

B_k	k th boundary segment.
C_p	Heat capacity.
E	Elastic modulus.
h_a	Heat transfer coefficient of air.
h_s	Heat transfer coefficient of solder.
k	Thermal conductivity.
t	Time.
T	Temperature.
T_∞	Far-field temperature.
$T_{\infty, a}$	Far-field air temperature.
$T_{\infty, s}$	Far-field solder process temperature.
u_i	i th component of displacement.
α	Thermal expansion coefficient.
ϵ_{ij}	$\partial u_i / \partial x_j$.
ν	Poisson's ratio.
ρ	Density.
σ_{ij}	Normal stress, i th component in j th direction.
σ_C	Principal compressive stress.
σ_T	Principal tensile stress.
σ_S	Principal shear stress.

I. INTRODUCTION

ALMOST ALL surface mounted circuits require the use of capacitors, either for electrical charge buffering or timing applications. The type of capacitor most often used is the surface mounted multilayer ceramic capacitor (MLCC). Unfortunately, several factors can cause MLCC failure. Thermal stress cracking associated with soldering operations is a major factor contributing to dropout rates of several

1000-ppm industry wide [1]. On a fundamental level, thermal stress cracking of MLCC's is caused by the inability of the MLCC to absorb stress, resulting from excessive temperature gradients. These stresses are caused by the mismatch of the mechanical and thermal properties of the constituent materials of the MLCC and the rate of change of temperature across the MLCC during movement through the solder wave.

A model of thermal stress development in surface mounted MLCC's was presented previously [2]. The model derivation and solution techniques are briefly reviewed in Section II of the current paper. This model was based on uncoupled, quasi-static thermoelastic theory and made use of both the actual geometry and mechanical and thermal properties of real MLCC printed wiring board (PWB). In the work reported here, numerical simulations are performed with the model. The model is used to investigate the effect of several important factors on the development of thermal stresses in MLCC's. These factors relate to the solder process temperature profile, MLCC geometry and material properties, and PWB material properties. These simulations are designed both to gain additional insight into the mechanism of thermal stress development and also to make recommendations on how to minimize the effects of thermal stresses, including thermal stress cracking.

Section III presents the results of the numerical simulation simulations. Section III-A introduces issues common to all of the simulations. Data analysis methods are discussed in Section III-B. The results of the base simulations are provided in Section III-C. The results of the solder process temperature profile simulations are presented in Section III-D. Section III-E presents the results obtained from the simulations designed to investigate MLCC termination materials and geometry. MLCC dielectric thickness simulation results are presented in Section III-F. MLCC electrode thickness and layer number simulation results are provided in Sections III-G and H, respectively. Section III-I presents the results of the MLCC dielectric bridge simulations.

The simulation results are discussed in Section IV. These results are compared to existing experimental work, and the functional relationships between the different simulation variables are discussed.

II. REVIEW OF MODEL: DERIVATION AND SOLUTION

A. Model: Derivation

Fig. 1 depicts the three-dimensional geometry of a typical MLCC. These capacitors consist of a block of ceramic dielectric material containing opposing sets of interleaved, planar, and metallic electrodes. Each set of electrodes ex-

Manuscript received September 7, 1989; revised May 30, 1990.

G. C. Scott is with the Engineering Research Center, AT&T Bell Laboratories, Princeton, NJ 08540.

G. Astfalk is with the Convex Computer Corporation, Greenbelt, MD 20770.

IEEE Log Number 9039125.

0148-6411/90/1200-1135\$01.00 © 1990 IEEE

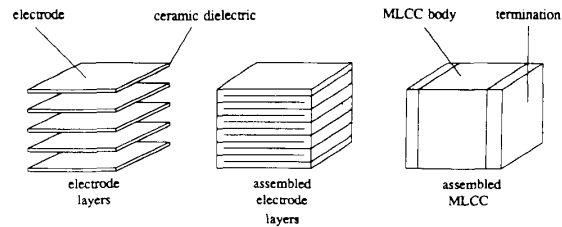


Fig. 1. Three-dimensional geometry of a typical MLCC.

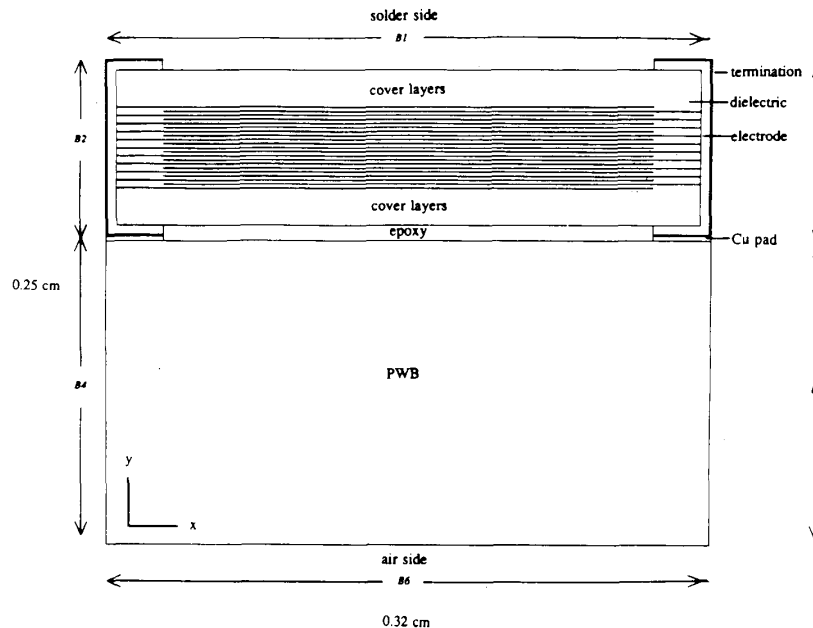


Fig. 2. Two-dimensional model domain sliced through the MLCC-PWB.

tends to two opposite surfaces of the MLCC where they are mated to an electrical termination. In order to make the problem tractable enough to obtain solutions in a timely fashion, the model was restricted to two dimensions sliced vertically through the MLCC and PWB as shown in Fig. 2. Both 1206 and 805 MLCC geometries were investigated with the model.

It was indicated previously [2] that the MLCC PWB structure is composed of several different materials. These materials generally include a dielectric, commonly a doped BaTiO_3 , 90/10 Ag/Pd electrode layers, terminations consisting of Ni, 90/10 Ag/Pd, and Sn-Pb layers, an adhesive, a Cu pad, and one of two different PWB materials, either FR-2 or FR-4. All of these materials have different mechanical and thermal parameters. The relevant mechanical parameters that are used in the model include E , the elastic modulus, ν , Poisson's ratio, and ρ , the density. Values of these parameters for each material type are provided in Table I. These values are usually temperature dependent. When possible, the temperature range for each value is also indicated in the table with the appropriate reference in square brackets. It was impossible to find values of the mechanical parameters for Ag-Pd. Therefore, values for Ag were used. Note that the major portion of the Ag-Pd alloy is Ag.

TABLE I
VALUES OF THE MECHANICAL PARAMETERS E , ν , AND ρ FOR THE DIFFERENT MLCC MATERIAL TYPES

Material	Mechanical Parameter					
	E , dyne/cm ²		ν		ρ , gm/cm ³	
dielectric	1.08×10^{12}	- [3]	0.33	- [17]	6.00	- [11]
electrode (Ag)	0.71×10^{12}	(350C) [4]	0.35	- [7]	10.50	- [12]
termination (Ni)	2.07×10^{12}	- [5]	0.26	(25-100C) [8]	8.91	(20C) [1]
termination (Sn-Pb)	0.33×10^{12}	- [5]	0.40	- [5]	10.19	- [5]
adhesive	0.10×10^{12}	- [9]	0.30	- [17]	2.67	- [13]
Cu pad	1.03×10^{12}	- [5]	0.33	- [5]	8.97	(20C) [5]
PWB (FR2)	0.38×10^{12}	- [6]	0.25	(25C) [10]	1.91	- [6]
PWB (FR4)	0.34×10^{12}	- [3]	0.25	- [10]	1.80	(154.4C) [14]

The relevant thermal parameters that are used in the model include C_p , the specific heat, k , the thermal conductivity, and α , the thermal expansion coefficient. Values of these thermal parameters are provided in Tables II-IV. These values are also temperature dependent. When possible, the temperature range for each value is also indicated in the table with the appropriate reference in square brackets. It was impossible to find values of the thermal parameters for the Ag-Pd layer of the termination. Therefore, values for Ag were used with the following exception. Values for k for a typical Ag-Pd alloy impregnated with glass frit were estimated by Rawal *et al.* [27] to be in the range of $10\text{--}25 \times 10^5$ erg/s-cm-C. Values of the heat transfer coefficients of solder

TABLE II
VALUES OF THE THERMAL PARAMETER C_p FOR THE DIFFERENT MLCC PWB MATERIAL TYPES

Material	Thermal Parameter		
	C_p , erg/gm-C		
dielectric	5.02×10^6	-	[11]
electrode (Ag)	2.39×10^6	(25C)	[12]
termination (Ni)	4.70×10^6	(0-100C)	[5]
termination (Sn-Pb)	1.29×10^6	(0C)	[5]
adhesive	4.00×10^6	-	[17]
Cu pad	$9.1 \times 10^2 T + 3.8 \times 10^6$	(20-1083C)	[5]
PWB (FR2)	7.10×10^6	-	[6]
PWB (FR4)	14.65×10^6	(25C)	[10]

TABLE III
VALUES OF THE THERMAL PARAMETER k FOR THE DIFFERENT MLCC PWB MATERIAL TYPES

Material	Thermal Parameter		
	k , erg/sec-cm-C		
dielectric	0.05×10^7	-	[11]
electrode (Ag)	$7.14 \times 10^3 T + 4.29 \times 10^7$	(0-260C)	[12]
termination (Ni)	0.86×10^7	(0-100C)	[5]
termination (Sn-Pb)	0.39×10^7	(15-100C)	[5]
adhesive	$5.5 \times 10^5, 1.9 \times 10^4$	$T < 70C, T \geq 70C$	[13]
Cu pad	$-7.80 \times 10^3 T + 4.10 \times 10^7$	(20-1083C)	[5]
PWB (FR2)	0.005×10^7	-	[14,15]
PWB (FR4)	0.005×10^7	(25C)	[14]

TABLE IV
VALUES OF THE THERMAL PARAMETER α FOR THE DIFFERENT MLCC PWB MATERIAL TYPES

Material	Thermal Parameter		
	α , /C		
dielectric	1.10×10^{-5}	-	[3]
electrode (Ag)	$7.20 \times 10^{-3} T + 1.90 \times 10^1$	(26.8-326.8C)	[8]
termination (Ni)	1.33×10^{-5}	(25-100C)	[5]
termination (Sn-Pb)	$26.50 \times 10^{-6} T$	(15-100C)	[5]
adhesive	12.00×10^{-5}	-	[13]
Cu pad	$7.97 \times 10^{-14} T^2 + 2.68 \times 10^{-10} T + 1.65 \times 10^{-5}$	(0-300C)	[5]
PWB (FR2)	1.85×10^{-5}	-	[15]
PWB (FR4)	1.44×10^{-5}	(0-125C)	[16]

and air, h_s and h_a , respectively, are important in the model. These values were taken to be 3.98×10^6 erg/s-cm²-C [17] and 1.50×10^4 erg/s-cm²-C [18] for solder and air, respectively.

Thermoelastic problems couple heat conduction and elastic deformation under transient conditions. The solution of two-dimensional thermoelastic problems typically consists of determining space-time dependent values of one temperature function, $T(x, y, t)$, two displacement functions, $u_x(x, y, t)$ and $u_y(x, y, t)$, four strain functions, $\epsilon_{xx}(x, y, t)$, $\epsilon_{yy}(x, y, t)$, $\epsilon_{xy}(x, y, t)$, and $\epsilon_{yx}(x, y, t)$, and four stress functions, $\sigma_{xx}(x, y, t)$, $\sigma_{yy}(x, y, t)$, $\sigma_{xy}(x, y, t)$, and $\sigma_{yx}(x, y, t)$. A conduction equation typically couples the strain and temperature fields. The displacement and stress fields are typically coupled through equations that include inertial terms. These equations together with stress-strain and strain-displacement equations form a suite of equations which describes a complex boundary value problem, whose solution is often difficult to obtain. It was demonstrated in [2], that under some general assumptions, the strain and

temperature fields can be uncoupled and that inertial effects can be ignored resulting in a quasi-static problem.

The complete two-dimensional uncoupled, quasi-static thermoelastic problem posed as a plane strain problem [19], [20] was then formulated to determine values of the following nine functions:

- 1) 1 temperature component: $T(x, y, t)$;
- 2) 2 displacement components: u_x, u_y ;
- 3) 3 strain components: $\epsilon_{xx}, \epsilon_{yy}, \epsilon_{xy}$;
- 4) 3 stress components: $\sigma_{xx}, \sigma_{yy}, \sigma_{xy}$.

So as to satisfy the following nine field equations throughout the MLCC and PWB.

- Heat conduction equation:

$$\rho C_p \frac{\partial T}{\partial t} - \frac{\partial}{\partial x} \left(k \frac{\partial T}{\partial x} \right) - \frac{\partial}{\partial y} \left(k \frac{\partial T}{\partial y} \right) = 0 \quad (1)$$

- 3 strain-displacement equations:

$$\epsilon_{xx} = \frac{\partial u_x}{\partial x} \quad (2)$$

$$\epsilon_{yy} = \frac{\partial u_y}{\partial y} \quad (3)$$

$$\epsilon_{xy} = \frac{1}{2} \left(\frac{\partial u_x}{\partial y} + \frac{\partial u_y}{\partial x} \right) \quad (4)$$

- 2 equilibrium equations:

$$\frac{\partial \sigma_{xx}}{\partial x} + \frac{\partial \sigma_{xy}}{\partial y} = 0 \quad (5)$$

$$\frac{\partial \sigma_{xy}}{\partial x} + \frac{\partial \sigma_{yy}}{\partial y} = 0 \quad (6)$$

- 3 stress-strain equations:

$$\sigma_{xx} = \frac{E}{(1+\nu)(1-2\nu)} [(1-\nu)\epsilon_{xx} + \nu\epsilon_{yy}] - \frac{\alpha E}{1-2\nu} (T - T_\infty) \quad (7)$$

$$\sigma_{yy} = \frac{E}{(1+\nu)(1-2\nu)} [\nu\epsilon_{xx} + (1-\nu)\epsilon_{yy}] - \frac{\alpha E}{1-2\nu} (T - T_\infty) \quad (8)$$

$$\sigma_{xy} = \frac{E}{(1+\nu)} (\epsilon_{xy}) \quad (9)$$

The above equations are solved subject to the appropriate initial and boundary conditions for the thermal and mechanical variables. The initial conditions are simply that the temperature field has a value of $T_{\infty,a}$ and that the displacement fields are zero at time 0. T_∞ is constant throughout time. $T_{\infty,a}$ is the far-field air temperature as opposed to $T_{\infty,s}$ which is the far-field solder temperature. These time varying temperatures are obtained from the temperature profiles of

the noncomponent side and the component side of the PWB, respectively, and are supplied to the temperature boundary conditions. The temperature profiles were determined by attaching thermocouples to the noncomponent side and the component side of the PWB and then processing the PWB through a wave soldering facility. The initial conditions are given in the following:

$$T(x, y, 0) = T_{\infty, a} \quad (10)$$

$$u_x(x, y, 0) = 0 \quad (11)$$

$$u_y(x, y, 0) = 0. \quad (12)$$

Fig. 2 defines six different boundary segments, B_1 – B_6 , over which the boundary conditions are defined. In general, one boundary condition relating to temperature and two boundary conditions relating to u_x and u_y must be defined for each boundary segment. Although the thermoelastic problem was posed as a plane strain problem, it will be solved as a displacement problem. Hence, the boundary conditions relating to the mechanics must be related to the displacement variables of each boundary segment.

1) *Temperature Boundary Conditions:* For boundary segment B_1 , a mixed Dirichlet–Neumann convective boundary condition is applied of the form

$$k \frac{\partial T}{\partial y} + h_s(T - T_{\infty, s}) = 0. \quad (13)$$

For boundary segments B_2 , a mixed Dirichlet–Neumann convective boundary condition is applied of the form

$$k \frac{\partial T}{\partial x} + h_s(T - T_{\infty, s}) = 0. \quad (14)$$

For boundary segments B_3 , a mixed Dirichlet–Neumann convective boundary condition is applied of the form

$$k \frac{\partial T}{\partial x} - h_s(T - T_{\infty, s}) = 0. \quad (15)$$

For boundary segments B_4 and B_5 , a Neumann boundary condition is applied of the form

$$\frac{\partial T}{\partial x} = 0. \quad (16)$$

This is simply a thermally insulated boundary condition. The heat flux across the sides of the PWB is assumed to be small and, thus insulated temperature boundary conditions are specified.

For boundary segment B_6 , a mixed Dirichlet–Neumann convective boundary condition is applied of the form

$$k \frac{\partial T}{\partial y} - h_s(T - T_{\infty, a}) = 0. \quad (17)$$

The above temperature boundary conditions specify that the temperature boundary conditions of the MLCC are a function of the solder bath temperature while the temperature boundary conditions of the PWB are insulated for *internal* boundaries and a function of the air temperature for the noncomponent side of the PWB.

2) *Mechanical Boundary Conditions:* For boundary segments B_1 , Neumann traction-free boundary conditions are applied of the form

$$\sigma_{yy} = 0 \quad (18)$$

$$\sigma_{xy} = 0. \quad (19)$$

For boundary segments B_2 and B_3 , Neumann traction-free boundary conditions are applied of the form

$$\sigma_{xx} = 0 \quad (20)$$

$$\sigma_{xy} = 0. \quad (21)$$

For boundary segments B_4 , B_5 , and B_6 , Dirichlet displacement-free boundary conditions are applied of the form

$$u_x = 0 \quad (22)$$

$$u_y = 0. \quad (23)$$

The above mechanical boundary conditions specify that the PWB is rigidly clamped to prevent any boundary displacements although the boundaries of the MLCC may experience some displacement while maintaining zero stress.

B. Model: Solution

The strategy for solving the above thermoelastic problem was discussed in [2]. Although several methods exist for solving the partial differential equations, the transient tensor Galerkin method for partial differential equations on rectangles (TTGR) solution method was selected [21]. This algorithm is similar to standard finite element methods in that the equations are solved on a mesh. The algorithm was implemented on a CONVEX C210 supercomputer. Solution times were approximately 120 CPU minutes.

III. RESULTS

A. Introduction

The model discussed previously was used to perform numerous simulations. The rationale, design, data analysis, and actual numerical results of these simulations are discussed in this section. These simulations were designed to investigate the effect of several important factors on the development of thermal stresses in MLCC's. These factors relate to the solder process temperature profile and MLCC PWB geometry and material properties.

There are at least two methods that can be used to interpret the simulation results. For each simulation, MLCC thermal stress levels in excess of a failure threshold stress level would imply that the MLCC is in mechanical failure. This constitutes a failure criterion. The model never explicitly accounts for crack development. Nonetheless, it is common practice to impose failure criteria without specifying the mechanism of failure. Many different failure criteria exist. Unfortunately, numerical threshold value of stress which cause failure in MLCC's are not well known. Hence, any failure criteria requiring knowledge of these values cannot be realistically imposed.

The second method that can be used to interpret the simulation results, and the one adopted here, is to specify a

set of base simulations. The levels of stress obtained from all other simulations can then be compared to the levels of stress obtained from these base simulations. The choice of a set of base simulations is arbitrary but this set should come from commonly encountered operating conditions which are known not to cause MLCC failure.

The second method for interpreting the simulation results is not as strong as the first. Higher levels of stress in the nonbase simulations compared to the base simulations is not sufficient to guarantee failure. In fact, failure cannot be assessed at all using the second method. The second method can point the way for performing laboratory experiments.

In the simulations designed to investigate factors related to MLCC PWB geometry, reference is made to *compensated* and *uncompensated* results. In the MLCC geometry, the dimensions of one material type can be changed at the expense of other material types to maintain overall MLCC package dimensions. The term *compensated* refers to this situation. Conversely, the dimensions of one material type can be changed while the dimensions of all other material types remain constant, thus changing the overall MLCC package dimensions. The term *uncompensated* refers to this situation. These two situations are important because they constitute two different approaches to manufacturing MLCC's.

B. Data Analysis

The output from TTGR consists of the temperature, T , axial displacements, u_x and u_y , normal strains ϵ_{xx} and ϵ_{yy} , shear strain ϵ_{xy} , normal stresses σ_{xx} and σ_{yy} , and shear stress σ_{xy} for each $x-y$ mesh point and for each time point requested by the user. In order to reference the normal and shear stresses from each simulation to a common set of axes, principal compressive, σ_C , principal tensile, σ_T , and principal shear, σ_S , stresses are calculated using

$$\sigma_C = \frac{\sigma_{xx} + \sigma_{yy}}{2} \pm \left[\left(\frac{\sigma_{xx} - \sigma_{yy}}{2} \right)^2 + \sigma_{xy}^2 \right]^{1/2} < 0 \quad (24)$$

$$\sigma_T = \frac{\sigma_{xx} + \sigma_{yy}}{2} \pm \left[\left(\frac{\sigma_{xx} - \sigma_{yy}}{2} \right)^2 + \sigma_{xy}^2 \right]^{1/2} > 0 \quad (25)$$

$$\sigma_S = \left[\left(\frac{\sigma_{xx} - \sigma_{yy}}{2} \right)^2 + \sigma_{xy}^2 \right]^{1/2} \quad (26)$$

The maximum principal stresses form the bulk of the reported data. Maximum values of the compressive, tensile, and shear principal stresses are reported. As an example of notation, the maximum compressive stress is denoted as $\sigma_{C, \max}$. The maximum value of the principal stress is provided for a particular mesh point within the MLCC PWB and at a particular time point in the temperature profile. The material type of the location of the maximum principal stress is also reported. The maximum value could be related to a failure criterion although such a criterion is not provided here for reasons discussed in Section III-A. Percent changes in the maximum principal stresses for the nonbase simulations relative to a particular base simulation are also reported. The

percent changes are calculated using

$$\Delta \sigma_{P, \max} = 100 \frac{\sigma_P(\text{nonbase}) - \sigma_P(\text{base})}{\sigma_P(\text{base})} \quad (27)$$

P denotes principal compressive, tensile, or shear stresses while "base" refers to a base simulation data and "nonbase" refers to a simulation data which is compared to the base simulation data. In the following, $\Delta \sigma_{P, \max}$ is denoted as $\Delta \sigma_{C, \max}$, $\Delta \sigma_{T, \max}$, or $\Delta \sigma_{S, \max}$ in reference to a specific principal stress, or more generally as $\Delta \sigma_{\max}$. The base simulations are numbered and this number is reported under the table column labeled "n" for each of the nonbase simulations in order to indicate the particular base simulation to which the nonbase simulation is compared. A positive value in the percent change is taken to mean a higher stress in the nonbase simulation compared to the base simulation. Particular results of the individual simulations are arbitrarily judged to be significant if at least a 10% change is registered for the maximum stress between the individual simulation and the particular base simulation.

C. Base Simulation

Fig. 3 is a temperature profile from the wave soldering facility soldering a surface mounted 1206 MLCC. This temperature profile and the 1206 geometry defined the first two base simulations, denoted as "WS-5" and "WS-2." "WS" denotes wave solder while "5" and "2" denotes 5- and 2-s time increments as explained in the following. The choice of a set of base simulations is arbitrary. The solder process temperature profile displayed in Fig. 3 comes from commonly encountered operating conditions which are known to not cause MLCC failure. The first base simulation used the entire temperature profile at a time resolution of 5 s, i.e., model output stress data every 5 s during the simulation. Finer resolution of 2 s was obtained during the second base simulation which used only the portion of the temperature profile corresponding to the solder wave. It was decided to concentrate on this portion of the temperature profile in some simulations because the peak stresses occur during this time. The decision is justified by the results presented in the next section. Also, finer time resolution increases the execution time of the simulation and a method had to be found to decrease this execution time from many hours to a few hours, the normal execution time of the first base simulation. In general, any comparison between a base simulation and a nonbase simulation implies that the same time resolution is present in both simulations.

Tables V-VII provide the summary data of the two base simulations for the principal compressive, tensile, and shear stresses, respectively. These tables also provide summary statistics for all of the nonbase simulations reported here.

D. Solder Process Temperature Profile Simulations

Four simulations were designed to investigate the influence of gradient and peak temperature of the preheat and solder process phases of the solder process temperature profile on the development of thermal stresses in MLCC's. Two addi-

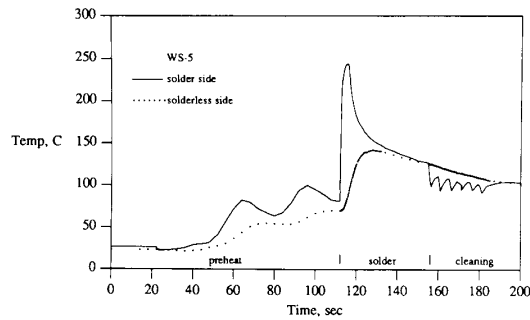


Fig. 3. Temperature profile from a wave soldering facility soldering a surface mounted discrete.

TABLE V
STATISTICS FOR THE MAXIMUM PRINCIPAL COMPRESSIVE STRESS DATA OF ALL SIMULATIONS

category	experiment	n	principal compressive stress		
			$\sigma_{C,max}$ Gdynes/cm ²	$\Delta\sigma_{C,max}$ %	location
base	WS-2	1	-1921.52	0.00	epoxy
	WS-5	2	-2368.76	0.00	epoxy
solder process temperature	WS-5	2	-2368.76	0.00	epoxy
	preheat-g	2	-2080.36	-12.18	PWB
	preheat-g+p	2	-2230.50	-5.84	dielectric
	solder-g	2	-1946.35	-17.83	dielectric
	solder-g+p	2	-1012.02	327.24	dielectric
	1/2 temp	2	-1618.22	-31.68	PWB
	Δ temp	2	-3194.81	34.87	epoxy
MLCC termination	2μm-c	1	-1926.39	0.25	dielectric
	6μm-c	1	-1988.72	3.50	electrode
	10μm-c	1	-2006.10	4.40	term: Ag-Pd layer
	14μm-c	1	-2011.09	4.66	term: Ag-Pd layer
	18μm-c	1	-2006.16	4.40	term: Ag-Pd layer
	2μm-u	1	-1926.39	0.25	dielectric
	6μm-u	1	-1988.72	3.50	electrode
	10μm-u	1	-2006.10	4.40	term: Ag-Pd layer
	14μm-u	1	-2011.09	4.66	term: Ag-Pd layer
	18μm-u	1	-2006.16	4.40	term: Ag-Pd layer
	Cu	1	-48.18	-97.49	PWB
	Ag	1	-50.25	-97.38	PWB
MLCC dielectric thickness	0.8-e+c	1	1911.75	-0.51	dielectric
	0.9-e+c	1	1914.82	-0.35	dielectric
	1.0-e+c	2	-1921.52	0.00	dielectric
	1.1-e+c	1	-1919.83	-0.09	epoxy
	1.2-e+c	1	-1921.77	0.01	PWB
	0.8-c	1	-1938.58	0.89	dielectric
	0.9-c	1	-1942.43	1.09	epoxy
	1.0-c	1	-1921.52	0.00	dielectric
	1.1-c	1	-1950.31	1.50	PWB
	1.2-c	1	-1952.48	1.61	PWB
MLCC electrode thickness	1μm-c	1	-1953.76	1.68	dielectric
	2μm-c	1	-1921.52	0.00	dielectric
	3μm-c	1	-1944.47	1.19	epoxy
	4μm-c	1	-1946.07	1.28	PWB
	5μm-c	1	-1947.17	1.33	epoxy
	1μm-u	1	-1951.90	1.58	dielectric
	2μm-u	1	-1921.52	0.00	dielectric
	3μm-u	1	-1947.70	1.36	PWB
	4μm-u	1	-1946.02	1.28	epoxy
	5μm-u	1	-1946.77	1.31	PWB
MLCC electrode layer number	10-c	1	-1922.75	0.06	PWB
	20-c	1	-1921.52	0.00	dielectric
	40-c	1	-1917.62	-0.20	electrode
	80-c	1	-1924.11	0.13	electrode
	10-u	1	-1937.12	0.81	dielectric
	20-u	1	-1921.52	0.00	dielectric
	40-u	1	-1967.46	2.39	dielectric
	80-u	1	-2000.19	4.09	dielectric
MLCC bridge design	twin 4	1	-1918.18	-0.17	dielectric
	twin 6	1	-1923.28	0.09	dielectric
	twin 8	1	-1922.11	0.03	dielectric

TABLE VI
STATISTICS FOR THE MAXIMUM PRINCIPAL TENSILE STRESS DATA OF ALL SIMULATIONS

category	experiment	n	principal tensile stress		
			$\sigma_{T,max}$ Gdynes/cm ²	$\Delta\sigma_{T,max}$ %	location
base	WS-2	1	3820.86	0.00	dielectric
	WS-5	2	4689.97	0.00	dielectric
solder process temperature	WS-5	2	4689.97	0.00	dielectric
	preheat-g	2	4110.93	-12.35	dielectric
	preheat-g+p	2	4370.53	-6.81	PWB
	solder-g	2	3968.01	-15.39	electrode
	solder-g+p	2	20189.10	330.47	dielectric
	1/2 temp	2	3200.22	-31.76	dielectric
	Δ temp	2	6279.26	33.89	dielectric
MLCC termination	2μm-c	1	3808.17	-0.33	dielectric
	6μm-c	1	1533.21	-59.87	PWB
	10μm-c	1	1448.69	-62.08	PWB
	14μm-c	1	1460.65	-61.77	PWB
	18μm-c	1	1488.18	-61.05	PWB
	2μm-u	1	3861.92	1.07	epoxy
	6μm-u	1	2933.16	-23.23	dielectric
	10μm-u	1	2166.06	-43.31	dielectric
	14μm-u	1	1711.00	-55.22	electrode
	18μm-u	1	1550.86	-59.41	PWB
	Cu	1	25.61	-99.33	dielectric
	Ag	1	28.79	-99.25	electrode
MLCC dielectric thickness	0.8-e+c	1	3770.69	-1.31	PWB
	0.9-e+c	1	3767.10	-1.41	dielectric
	1.0-e+c	2	3820.86	0.00	dielectric
	1.1-e+c	1	3758.01	-1.64	dielectric
	1.2-e+c	1	3752.74	-1.78	dielectric
	0.8-c	1	3872.59	1.35	dielectric
	0.9-c	1	3872.32	1.35	electrode
MLCC electrode thickness	1.0-c	1	3820.86	0.00	dielectric
	1.1-c	1	3873.64	1.38	dielectric
	1.2-c	1	3875.50	1.43	dielectric
	1μm-c	1	3866.67	1.20	PWB
	2μm-c	1	3820.86	0.00	dielectric
	3μm-c	1	3874.74	1.41	dielectric
	4μm-c	1	3873.90	1.39	dielectric
	5μm-c	1	3875.34	1.43	epoxy
	1μm-u	1	3863.19	1.11	PWB
	2μm-u	1	3820.86	0.00	dielectric
MLCC electrode layer number	3μm-u	1	3876.65	1.46	dielectric
	4μm-u	1	3826.10	0.14	electrode
	5μm-u	1	3878.84	1.52	PWB
	10-c	1	3822.95	0.05	PWB
	20-c	1	3820.86	0.00	dielectric
	40-c	1	3762.68	-1.52	dielectric
	80-c	1	3825.34	0.12	electrode
	10-u	1	3860.85	1.05	PWB
MLCC bridge design	20-u	1	3820.86	0.00	dielectric
	40-u	1	3886.05	1.71	electrode
	80-u	1	3974.31	4.02	electrode
	twin 4	1	3779.23	-1.09	dielectric
	twin 6	1	3811.38	-0.25	dielectric
	twin 8	1	3808.08	-0.33	electrode

tional simulations were designed to investigate the influence of the peak temperature of the solder process phase and the difference in temperature between the temperature at the end of the preheat phase and the peak temperature of the solder process phase on the development of thermal stresses in MLCC's. The base 1206 MLCC geometry and adjusted versions of the "WS" solder process temperature profile were used in these simulations. The results of these simulations are discussed in the following. Solder process temperature profiles are provided in Figs. 4-9.

Fig. 4 depicts a 100% increase in the preheat phase temperature gradient for the "WS" solder process temperature profile displayed in Fig. 3. This was accomplished by reducing the time base of the preheat phase temperature by 50%. Note that the peak temperatures of the preheat phase

TABLE VII
STATISTICS FOR THE MAXIMUM PRINCIPAL SHEAR STRESS DATA OF ALL
SIMULATIONS

category	experiment	n	principal shear stress		
			$\sigma_{s,max}$ Gdynes/cm ²	$\Delta\sigma_{s,max}$ %	location
base	WS-2	1	1321.92	0.00	term: Sn-Pb layer
	WS-5	2	1622.52	0.00	term: Sn-Pb layer
process temperature profile	preheat-g	2	1420.28	-12.46	term: Sn-Pb layer
	preheat-g+p	2	1518.40	-6.42	term: Sn-Pb layer
	solder-g	2	1369.43	-15.60	term: Sn-Pb layer
	solder-g+p	2	6990.35	330.83	term: Sn-Pb layer
	1/2 Δ temp	2	1106.45	-31.81	term: Sn-Pb layer
	Δ temp	2	2181.05	34.42	term: Sn-Pb layer
MLCC termination	2 μ m-c	1	1315.11	-0.52	term: Sn-Pb layer
	6 μ m-c	1	728.75	-44.87	term: Ni layer
	10 μ m-c	1	552.75	-58.19	term: Ni layer
	14 μ m-c	1	516.83	-60.90	solder pad
	18 μ m-c	1	500.72	-62.12	solder pad
	2 μ m-u	1	1333.68	0.89	term: Sn-Pb layer
	6 μ m-u	1	955.46	-27.72	term: Sn-Pb layer
	10 μ m-u	1	705.41	-46.64	term: Sn-Pb layer
	14 μ m-u	1	559.69	-57.66	term: Sn-Pb layer
	18 μ m-u	1	498.55	-62.29	solder pad
	Cu	1	15.02	-98.86	term: Sn-Pb layer
	Ag	1	15.56	-98.82	solder pad
MLCC dielectnc thickness	0.8-e+c	1	1313.58	-0.63	term: Sn-Pb layer
	0.9-e+c	1	1311.01	-0.83	term: Sn-Pb layer
	1.0-e+c	2	1321.92	0.00	term: Sn-Pb layer
	1.1-e+c	1	1305.07	-1.27	term: Sn-Pb layer
	1.2-e+c	1	1301.82	-1.52	term: Sn-Pb layer
	0.8-c	1	1344.44	1.70	term: Sn-Pb layer
	0.9-c	1	1342.06	1.52	term: Sn-Pb layer
	1.0-c	1	1321.92	0.00	term: Sn-Pb layer
MLCC electrode thickness	1.1-c	1	1339.33	1.32	term: Sn-Pb layer
	1.2-c	1	1337.27	1.16	term: Sn-Pb layer
	1 μ m-c	1	1338.40	1.25	term: Sn-Pb layer
	2 μ m-c	1	1321.92	0.00	term: Sn-Pb layer
	3 μ m-c	1	1340.71	1.42	term: Sn-Pb layer
	4 μ m-c	1	1338.98	1.29	term: Sn-Pb layer
	5 μ m-c	1	1341.63	1.49	term: Sn-Pb layer
	1 μ m-u	1	1340.99	1.44	term: Sn-Pb layer
MLCC electrode layer number	2 μ m-u	1	1321.92	0.00	term: Sn-Pb layer
	3 μ m-u	1	1341.96	1.52	term: Sn-Pb layer
	4 μ m-u	1	1329.36	0.56	term: Sn-Pb layer
	5 μ m-u	1	1342.31	1.54	term: Sn-Pb layer
	10-c	1	1324.12	0.17	term: Sn-Pb layer
	20-c	1	1321.92	0.00	term: Sn-Pb layer
	40-c	1	1308.18	-1.04	term: Sn-Pb layer
	80-c	1	1325.09	0.24	term: Sn-Pb layer
MLCC bridge design	10-u	1	1338.19	1.23	term: Sn-Pb layer
	20-u	1	1321.92	0.00	term: Sn-Pb layer
	40-u	1	1350.61	2.17	term: Sn-Pb layer
	80-u	1	1377.46	4.20	term: Sn-Pb layer
MLCC bridge design	twin 4	1	1318.86	-0.23	term: Sn-Pb layer
	twin 6	1	1329.22	0.55	term: Sn-Pb layer
	twin 8	1	1328.17	0.47	term: Sn-Pb layer

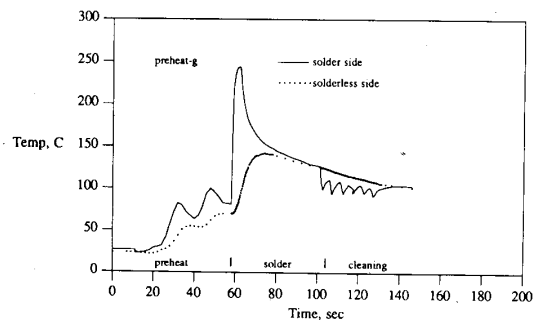


Fig. 4. Temperature profile from Fig. 3 with the preheat temperature time base reduced by 50%.

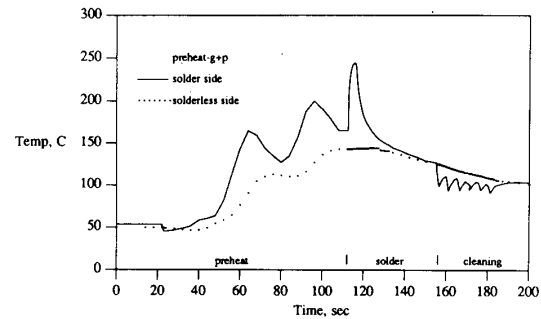


Fig. 5. Temperature profile from Fig. 3 with the preheat temperature magnitude and time base increased by 100%.

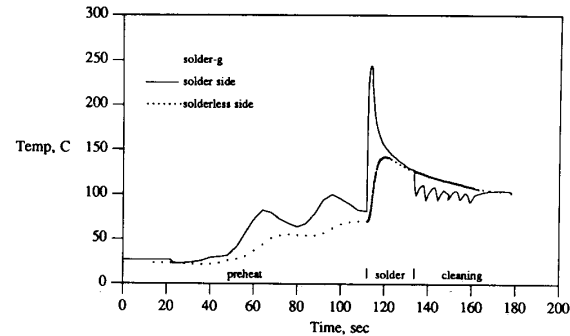


Fig. 6. Temperature profile from Fig. 3 with the solder process temperature time base reduced by 50%.

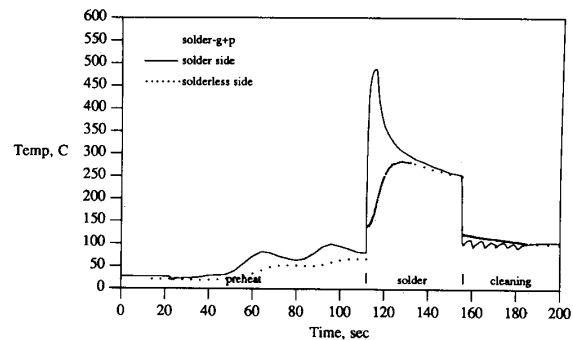


Fig. 7. Temperature profile from Fig. 5 with the solder process temperature magnitude and time base increased by 100%.

are the same in both figures. The stress data for the model run using this profile is referenced in Tables V-VII as "preheat-g" for preheat temperature gradient changes.

Fig. 5 depicts a 100% increase in the preheat phase temperature gradient and a 100% increase in the temperatures of the preheat phase for the "WS" solder process temperature profile displayed in Fig. 3. The stress data for the model run using this profile is referenced in Tables V-VII as "preheat-g + p" for preheat temperature gradient and peak temperature changes.

Fig. 6 depicts a 100% increase in the solder process phase temperature gradient for the "WS" solder process temperature profile displayed in Fig. 3. This was accomplished by reducing the time base of the solder process phase tempera-

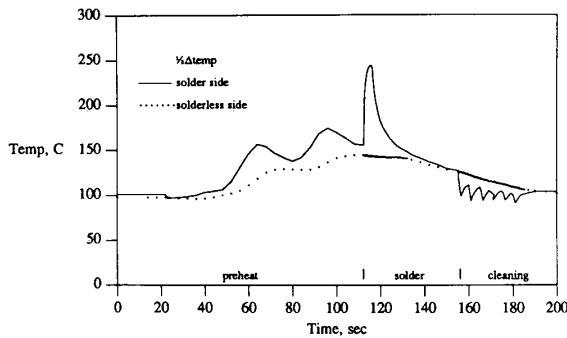


Fig. 8. Temperature profile from Fig. 3 with the change in temperature between the end of preheat temperature and the peak temperature during solder process reduced by 50%. Note that this was accomplished by scaling the preheat temperature, not by scaling the peak temperature during solder.

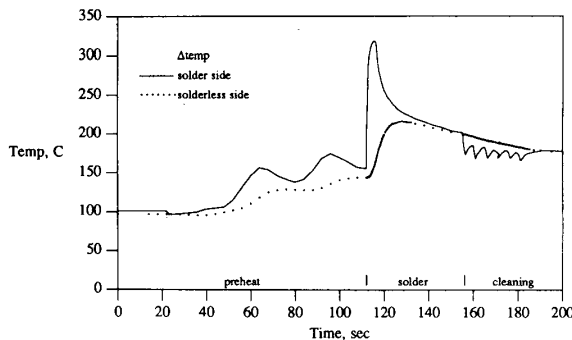


Fig. 9. Temperature profile from Fig. 3 with the same change in temperature as displayed in Fig. 7 between the end of preheat temperature and the peak temperature during solder process. Note that this change was restored compared to Fig. 8 by scaling the solder process temperatures, not the preheat temperatures. The same preheat temperatures are depicted in this figure as in Fig. 7.

ture by 50%. Note that the peak temperatures of the solder process phase are the same in both figures. The stress data for the model run using this profile is referenced in Tables V-VII as "solder-g" for solder process temperature gradient changes.

Fig. 7 depicts a 100% increase in the solder process phase temperature gradient and a 100% increase in the temperatures of the solder process phase for the "WS" solder process temperature profile displayed in Fig. 3. The stress data for the model run using this profile is referenced in Tables V-VII as "solder-g + p" for solder process temperature gradient and peak temperature changes.

Fig. 8 depicts a 50% decrease in the change in temperature between the temperature at the end of the preheat phase and the peak temperature of the solder process phase. This was accomplished by elevating the temperatures of the preheat phase. Note that the peak temperature of the solder process phase and the gradients of both the preheat phase and solder process phase are the same as depicted in Fig. 3. The stress data for the model run using this profile is referenced in Tables V-VII as " $1/2\Delta\text{temp}$."

Fig. 9 depicts a temperature profile in which the change in temperature between the temperature at the end of the preheat

phase and the peak temperature of the solder process phase has been restored to its original value depicted in Fig. 3. Note that this was accomplished by elevating the temperatures of the solder phase. The temperatures of the preheat phase are at the same level as they were in Fig. 9. The stress data for the model run using this profile is referenced in Tables V-VII as " Δtemp ."

The data of the solder process temperature profile simulations indicate that the combination of increases in both solder process gradient and peak temperature yield some of the greatest increases in the levels of all of the principal stresses for any of the simulations performed in this study. The data for the remaining conditions in this set of simulations (e.g., conditions of preheat) display mixed significance. These data generally display lower magnitudes of change relative to the data of the base simulation than the corresponding data for the conditions of the solder process gradient and peak temperature.

E. MLCC Termination Simulations

A simulation was designed to investigate the influence of the Ni layer thickness of the MLCC termination and all Cu and all Ag MLCC terminations on the development of thermal stresses in MLCC's. Nominal Ni layer thicknesses of 2, 6, 10, 14, and 18 μm were tested for both compensated and uncompensated MLCC geometries. The Ag-Pd layer of the MLCC termination was used as the compensating material type for the Ni layer. The base 1206 MLCC geometry and the "WS" solder process temperature profiles were used in these simulations. The stress data for Ni layer thickness simulations are referenced in the tables by the nominal Ni layer thickness with a suffix of "-c" denoting compensated data and a suffix of "-u" denoting uncompensated data. The stress data for the all Cu and Ag termination simulations are referenced in the tables with the terms "Cu" and "Ag."

The MLCC termination simulations yielded data that generally indicate that thicker Ni layers are associated with lower values of stress. All of the data for the Cu and Ag termination simulations were significantly less than the data of the base simulations.

F. MLCC Dielectric Thickness Simulations

The thickness of the dielectric layers may influence the development of thermal stresses in MLCC's. There are two different dielectric layers of equal thickness in the base 1206 geometry: one type of layer is associated with each electrode layer and another type is associated with each cover layer. Nominal dielectric layer thicknesses of 0.8x, 0.9x, 1.0x, 1.1x, and 1.2x the thickness of the dielectric layer of the base 1206 geometry was tested. The stress data for the model runs are referenced by the multiplicative factors discussed above with a suffix of "-e + c" for the simulations in which the electrode layer and cover layer dielectric thicknesses were changed and by "-c" for the simulations in which just the cover layer dielectric thicknesses were changed.

No significant changes were recorded in the individual results of dielectric layer thickness simulations.

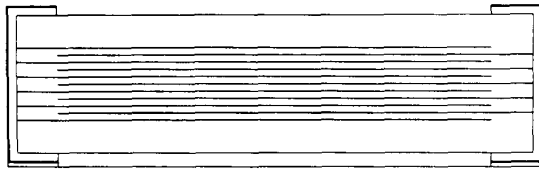


Fig. 10. Compensated 10 electrode layer MLCC geometry.

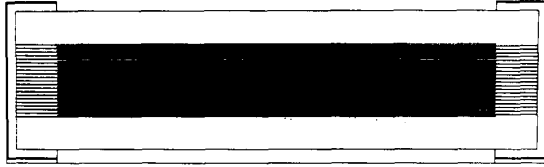


Fig. 11. Compensated 40 electrode layer MLCC geometry.

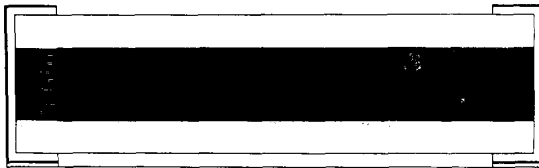


Fig. 12. Compensated 80 electrode layer MLCC geometry.

G. MLCC Electrode Thickness Simulations

Just as the thickness of the dielectric layers may influence the development of thermal stresses in MLCC's, the thickness of the electrodes may have a similar influence. Nominal electrode thicknesses of 1, 2, 3, 4, and 5 μm were tested for both compensated and uncompensated MLCC geometries. The dielectric layer of the MLCC electrode layer was used as the compensating material type for each electrode. The base 1206 MLCC geometry and the "WS" solder process temperature profile were used in these simulations.

No significant changes were recorded in the individual results of the MLCC electrode thickness simulations. Changes in the maximum stresses between the individual simulations and base simulations were less than 2.0%. There appear to be few consistent patterns in the individual results of these simulations.

H. MLCC Electrode Layer Number Simulations

A simulation was designed to investigate the influence of the number of electrode layers on the development of thermal stresses in MLCC's. Nominal electrode layer numbers of 10, 20, 40, and 80 for both compensated and uncompensated MLCC geometries were investigated. The dielectric layer of the MLCC electrode layer was used as the compensating material type for each layer. The base 1206 MLCC geometry and the "WS" solder process temperature profile were used in these simulations.

Figs. 10–12 depict the compensated MLCC geometries for 10, 40, and 80 electrode layers. The 20 electrode layer is the base 1206 geometry depicted in Fig. 2. The compensated geometries were similar to those depicted except that a constant thickness of the base 1206 geometry was used for the dielectric layer thickness.

The stress data for the model runs are referenced in Tables V–VII by the nominal electrode thicknesses with a suffix of

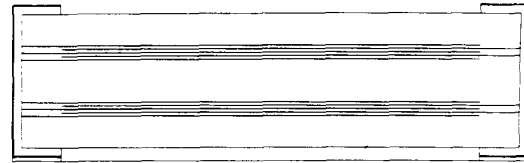


Fig. 13. Twin four electrode layer bridge MLCC geometry.

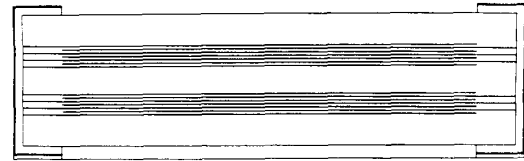


Fig. 14. Twin six electrode layer bridge MLCC geometry.

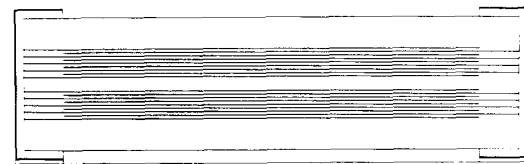


Fig. 15. Twin eight electrode layer bridge MLCC geometry.

"-c" for the compensated data and "-u" for the uncompensated data.

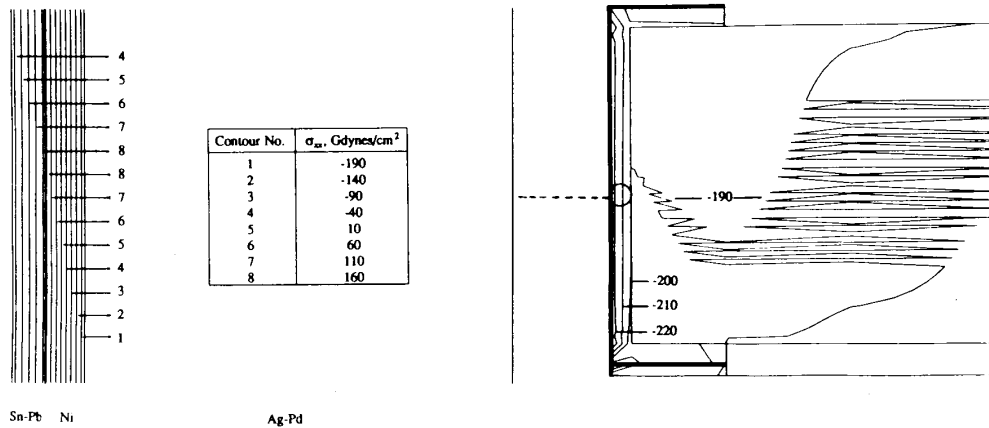
In the MLCC electrode layer number simulations, none of the maximum principal stresses were judged to be significant. Several interesting patterns exist in these data even though all of the data fall below the level of change judged to be significant. Both the compensated and uncompensated results display similar patterns, although the changes in the stress data compared to the base simulation stress data are greater for the uncompensated results. Generally, $\Delta\sigma_{\text{max}}$ has the highest value for the highest number of electrode layers.

I. MLCC Bridge Design Simulations

In recent years, bridge design MLCC geometries have been devised to reduce thermal stresses in MLCC's [27]. Bridge design MLCC geometries include a central dielectric layer which separates the electrode layers into identical upper and lower layer groups. These designs are referred to as twin electrode layer bridges in the following. Twin four, six, and eight electrode layer bridge geometries were investigated. These designs were formed by replacing an appropriate number of centrally located electrode layers of the base 1206 MLCC geometry with dielectric layers. The base 1206 MLCC geometry and the "WS" solder process temperature profile were used in these simulations.

Figs. 13–15 depict the bridge design MLCC geometries for the twin four, six, and eight electrode layer bridges.

No significant changes were recorded in the individual results of the MLCC bridge design simulations. Nonetheless, it is interesting that all of the values $\Delta\sigma_{C, \text{max}}$ are all positive for all bridge designs, with the twin 4 design displaying the greatest change relative to the base simulation. Just the opposite is true for all the values $\Delta\sigma_{T, \text{max}}$. These values are all negative for all bridge designs, with the twin 8 design displaying the greatest change relative to the base simulation.



termination

Fig. 16. Representative contour levels of σ_{xx} within the MLCC. The left-hand side of the figure is a magnification of the central portion of the left termination as indicated. Note the change of contour scale between the right- and left-hand sides.

IV. DISCUSSION

A model of thermal stress development in MLCC's has been presented. This model included the specific geometry and material properties of the MLCC PWB structure as well as the thermal environment to which this structure is exposed.

When possible, the results of any numerical model should be compared to controlled experimental results. That is, some form of validation should be included in the development of the model. Frequently, this comparison is limited by the lack of extensive experimental results. Such is the case in the current effort. Nonetheless, five references to independent experimental work exist to which the results of the current study can be compared.

The magnitudes of the calculated stresses reported here are in the same range as those reported as MLCC failure stresses in the experimental literature. McKinney *et al.* [22] report failure stresses for commercially available MLCC's in the range of 104.8–251.8 Gdynes/cm². Pollock *et al.* [23] report failure stresses for several 805 MLCC's in the approximate range of 100–250 Gdynes/cm². Many of the results reported here are in this same range. In particular, values of the maximum stresses are in the range starting at approximately 100 Gdynes/cm² and extending to stress values frequently at least an order of magnitude greater. It should be noted that the data reported by McKinney *et al.* and Pollock *et al.* is from mechanically, not thermally, induced MLCC failures. Unfortunately, similar data for thermally induced failures does not appear to be available in the experimental literature.

Fig. 16 depicts contour levels of σ_{xx} within the MLCC. The electrodes have been removed to more clearly depict the stress contour levels of the central portion of the MLCC. These results were obtained at 44 s for base simulation 1 and are fairly typical of those observed in many of the other simulations. Base and increment contour values are at -220.0 and 10.0 Gdynes/cm², respectively. Note that the contour

lines frequently run perpendicular to the thickness of the MLCC close to the terminations and frequently parallel the electrode-dielectric interface away from the terminations. It is expected that actual cracking failure of these portions of the MLCC under thermal load would extend along the most extreme of these contour lines. In fact, Van Den Avyle *et al.* [24], McKinney *et al.* [22], and Evans *et al.* [25] report experimental MLCC failure geometries which are similar to the stress contour geometries depicted in Fig. 16. Interfacial fractures of adhesively bonded materials under different conditions of stress are well known in the field of fracture mechanics [26].

The work reported by Rawal *et al.* [27] in a corporate technical information bulletin consisted of an experimental study of the thermal shock behavior of several prepared samples of MLCC's with different dielectric compositions and geometric designs. Three of the six factors studied in the work reported here were also studied by Rawal *et al.* including termination Ni layer thickness, electrode and cover layer dielectric thickness, and bridge design. Several of the results reported by Rawal *et al.* conflict with those reported here. Reasons for these discrepancies are discussed in the following.

Rawal *et al.* indicate a trend in thermal stress development which is opposite to that reported here for the same range of Ni layer thicknesses. They tested samples of 1206, 1210, and 1812 size MLCC's although Ni layer thicknesses are quoted only for the 1812 sizes. For instance, out of lots of 50 1812 MLCC's tested for each change in Ni layer thickness, 2 samples developed visible cracks for Ni layer thicknesses under approximately 4.80 μm , while 5 samples each developed visible cracks at 8.70 and 18.41 μm Ni layer thicknesses. This is the single discrepancy between their results and the results reported here that cannot be explained.

Rawal *et al.* report an increase in the number of visible cracks for increases in the dielectric thickness in the range of 5–229 μm in 1210 MLCC samples. In contrast, no signifi-

cant changes in thermal stress development were observed in the work reported here. The following reasons account for this discrepancy. The cover layer and overall MLCC thickness were held constant in their study. The only manner in which to achieve this is to increase the number of electrode layers while at the same time decreasing the thickness of the dielectric layer associated with each electrode. Their results may be confounded by an increase in the number of electrodes.

The study of both electrode and cover layer dielectric thicknesses reported here changed the overall thicknesses of the MLCC. This could also account for the discrepancy in the results discussed above. However, Rawal *et al.* also report results on the effect of changes in MLCC thickness on cracking. Their results indicate the presence of visible cracks for MLCC thickness changes in the range of 1.01–1.52 mm although they do not indicate how the thickness changes were accomplished.

Rawal *et al.* report a significant decrease in the number of visible cracks for bridge design MLCC's compared to non-bridge designs. In contrast, the work reported here indicates no significant change in thermal stress development. Unfortunately, Rawal *et al.* do not report information that allows comparisons of geometry. Furthermore, the thermal environments to which the MLCC's were exposed in their bridge design simulations was 425°C, significantly higher than in the work reported here.

The material type at the location of the maximum principal stress for each simulation was reported in Section III. Apparent patterns to these locations include the following. As reference points to horizontal locations within the MLCC, divide the cross section of the MLCC into quarters with lines joining the solder and PWB surfaces. Then:

- $\sigma_{C, \max}$ typically was located within the right or left most 25% region of the MLCC;
- $\sigma_{T, \max}$ typically was located within the middle 50% region and frequently close to the vertical center line of the MLCC;
- $\sigma_{S, \max}$ was located typically in the Sn–Pb or Ni layer of the termination;
- there was a great variation in the vertical location of all three stresses between simulations.

V. CONCLUSION

A model to characterize the development of thermal stresses in surface mounted MLCC's was presented in [2]. The work reported here concerned numerical simulations using this model. In particular, the model was used to investigate the effect of several important factors on the development of thermal stresses in MLCC's. These factors relate to the solder process temperature profile and MLCC PWB geometry and material properties. The results indicate that the peak temperature during wave solder and that the geometry and material properties of the MLCC termination have a major influence on the development of thermal stresses in MLCC's.

These factors are actually a small portion of all of the factors investigated in this work.

ACKNOWLEDGMENT

Linda Kaufman made several substantial reductions in the execution time of TTGR during the course of this project. George Wenger provided access to the majority of the solder process and IR temperature profiles used in the simulations.

REFERENCES

- [1] A. Danford and G. Marten, "Ceramic chip capacitor thermal shock experiment," Tech. Rep., Hewlett-Packard Co., p. 17, 1988.
- [2] G. C. Scott and G. Astfalk, "Modeling thermal stress behavior in microelectronic components," *ASME J. Electron. Pack.*, vol. 112, pp. 35–40, 1989.
- [3] Murata, *Monolithic Ceramic Capacitor Application Manual*, 1987, p. 13.
- [4] T. Lyman, ed., *Metals Handbook: Vol. 1: Properties and Selection of Metals*. Novelty: OH, 1961, p. 1182.
- [5] S. L. Hoyt, ed., *ASME Handbook of Metals Properties*. New York: McGraw Hill, 1954, pp. 299, 300, 371, 392, 395.
- [6] R. H. Perry and C. H. Chilton, eds., *Chemical Engineers' Handbook*. New York: McGraw-Hill, 1973, pp. 26–63.
- [7] G. Basile, G. Martini, and G. Zosi, "X-ray determination of the Poisson's ratio in thin films," *Thin Solid Films*, vol. 11, pp. 441–443, 1972.
- [8] C. T. Lynch, ed., *CRC Handbook of Materials Science, Vol. II: Metals, Composites, and Refractory Materials*. Boca Raton, FL: CRC, 1984, pp. 123, 218.
- [9] —, *CRC Handbook of Materials Science, Vol. III: Nonmetallic Materials and Applications*. Boca Raton, FL: CRC, 1984, p. 21.
- [10] J. Yuan, personal communications, AT&T Bell Laboratories, 1988.
- [11] H. C. Ling, personal communication, AT&T Bell Laboratories, 1986.
- [12] R. C. Weast, *Handbook of Chemistry and Physics*, 60th ed. Cleveland, OH: CRC, 1979, pp. B-134, D-141, E-10.
- [13] "Specification sheet for EPO-TEK H70E-4," Epoxy Technology, Inc., 1983.
- [14] J. Maxwell, "Cracks: The hidden defect," Tech. Rep., AVX Corp., p. 1, 1988.
- [15] C. F. Coombs, Jr., *Printed Circuits Handbook*, 3rd ed. New York: McGraw Hill, 1988, p. 6.28, 6.31.
- [16] "Electronics," p. 80, Nov. 27, 1986.
- [17] R. Mahajan, personal communication, AT&T Bell Laboratories, 1988.
- [18] J. P. Holman, *Heat Transfer*. New York: McGraw Hill, 3rd ed., 1972, p. 12.
- [19] Y. C. Fung, *Foundations of Solid Mechanics*. Englewood Cliffs, NJ: Prentice-Hall, 1965, pp. 233–234.
- [20] D. J. Johns, *Thermal Stress Analysis*. New York: Pergamon, 1965, pp. 24–26.
- [21] L. Kaufman and N. L. Schryer, "Solving 2-dimensional partial differential equations on vector and scalar machines," *Int. J. Supercomput. Applications*, vol. 3, no. 1, pp. 10–33, 1989.
- [22] K. R. McKinney, R. W. Rice, and C. C. Wu, "Mechanical failure characteristics of ceramic multilayers capacitors," *J. Amer. Ceram. Soc.*, vol. 69, no. 10, p. C-228, 1986.
- [23] K. L. Pollock and C. E. Hodgkins, "Fracture strength of multilayer ceramic capacitors," in *Proc. Int. Symp. on Microelectronics*, 1984, pp. 450–456.
- [24] J. A. Van Den Avyle and J. J. Mecholsky, "Analysis of soldering-induced cracking of BaTiO₃ ceramic capacitors," *Ferroelectrics*, vol. 50, pp. 293–298, 1983.
- [25] A. G. Evans and M. Ruhle, "On the mechanics of failure in ceramic/metal bonded systems," in *Mat. Res. Soc. Symp. Proc.*, vol. 40, 1985, pp. 153–166.
- [26] M. D. Thouless, "The role of fracture mechanics in adhesion," in *Mat. Res. Soc. Symp. Proc.*, vol. 119, 1988, pp. 51–62.
- [27] B. S. Rawal, R. Ladew, and R. Garcia, "Factors responsible for thermal shock behavior of chip capacitors," *Tech. Info. Bull.*, AVX Corp., pp. 1–8, 1987.